SUPPORTING INFORMATION

Uncovering single-molecule photophysical heterogeneity of bright, thermally-activated delayed fluorescence emitters dispersed in glassy hosts

Rodrigo Noriega[1,2], Edward S. Barnard[3], Benedikt Ursprung[3], Benjamin L. Cotts[1], Samuel B. Penwell[1], P. James Schuck[3], Naomi S. Ginsberg[*,1,2,4,5,6]
[1]Department of Chemistry and [4]Department of Physics, University of California Berkeley, Berkeley, California 94720, United States
[2]Materials Sciences Division, [3]The Molecular Foundry, and [5]Molecular Biophysics and Integrative Bioimaging Division, Lawrence Berkeley National Laboratory, Berkeley, California 94720, United States
[6]Kavli Energy NanoSciences Institute, Berkeley, California 94720, United States
* Corresponding author. Email: nsginsberg@berkeley.edu

A. Methods and Materials

Sample preparation. Nexterion glass coverslips, glass microscope slides and all glassware used in the preparation of solutions were sonicated for 15 minutes in successive baths of acetone, isopropyl alcohol, 2% Hellmanex solution in NANOpure deionized water, and 2X rinses in NANOpure deionized water, and immediately dried with filtered N_2 flow. Coverslips and microscope slides were further cleaned with O_2 plasma in a reactive ion etch chamber. Glassware was baked at 450 ºC under continuous Ar flow. Magnetic spinbars for solution stirring and Teflon vial caps were cleaned in an identical manner, minus the plasma and baking steps. All materials were brought to a sealed glove box with N_2 atmosphere (< 2 ppm H_2O, < 10 ppm O_2). PMMA (Aldrich, M_w≈350,000), polystyrene (Aldrich, M_w≈280,000), chlorobenzene (Sigma-Aldrich), and 2PXZ-OXD (Lumtec) were used as received. Polymer solutions (20 mg/mL) and a $2x10^{-2}$ M solution of 2PXZ-OXD were stirred overnight and filtered through a 0.45 µm pore size syringe filter prior to film preparation. The $2x10^{-2}$ M emitter stock solution was sequentially diluted in chlorobenzene to reach a $2x10^{-12}$ M concentration, mixed with the host polymer solution in equal volume to yield the final preparation (10 mg/mL host and 10^{-12} M emitter), of which 250 µL were pipetted onto a clean coverslip and spun at 10,000 rpm for 2 min. Dry samples were encapsulated between the coverslip and microscope slides with UV-curable epoxy (EPO-TEK ®) and exposed to 254 nm UV light, protecting the sample active area with a mask.

Microscope setup. The output of a Coherent Mira 900 oscillator tuned to 830 nm (150 fs pulse duration, 75.9 MHz repetition rate) was frequency-doubled in a BBO crystal, filtered with a 750 nm shortpass dichroic (Semrock) and a 425 nm shortpass filter (Chroma), and its power adjusted with a variable neutral density filter. The excitation beam was directed to a Nikon Eclipse Ti-U microscope with a Nikon 100X NA=1.4 oil immersion objective in the epifluorescence configuration. For single-molecule measurements of 2PXZ-OXD embedded in PMMA, the beam waist was 0.75 µm and the excitation beam power was 2.4 µW ($3.16x10^{-14}$ J/pulse) at the back of the objective; for measurements of 2PXZ-OXD embedded in polystyrene, the beam waist was 1.3 µm and the excitation beam power was 15 µW ($1.98x10^{-13}$ J/pulse) at the back of the objective. The excitation beam was linearly polarized, and the polarization was kept constant throughout the experiments. Spatial filtering to reduce the anisotropic beam mode of the

excitation laser would have significantly reduced its power and was not employed; using a beam therefore somewhat larger than the diffraction limit was not an issue due to the low density of emitters in the sample. Photoluminescence was collected through a 430 nm longpass dichroic and 430 nm longpass filter (Chroma). Spectrally-resolved data was collected with an Acton 2300i spectrometer (150 grooves/mm) and an Andor iXon CCD camera with a 30 s integration time and dark background subtraction, which involves substantially more time-averaging over fluctuations than the 2-s time bins used in time-resolved PL analysis. Due to blinking, some emitters were not in a bright state during the collection of emission spectra. Time-resolved data was collected with a Micro Photon Devices PDM series single-photon avalanche photodiode and a PicoQuant PicoHarp 300 time-correlated single-photon counting system. The instrument response function of the time-resolved setup has a full-width at half maximum of 192 ps, as shown in Fig. S1.

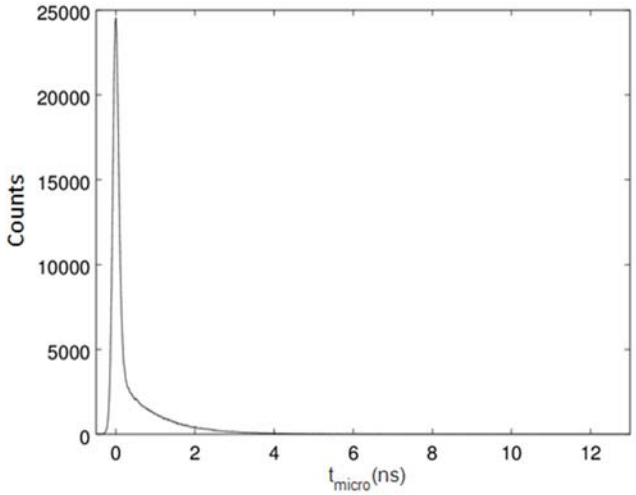

Figure S1. Instrument response function of the time-resolved data acquisition, with a full-width at half-maximum of 192 ps

Bulk spectroscopic measurements. Films prepared identically to those used in single-molecule studies but with a 10^{-3} M 2PXZ-OXD solution were used to measure ensemble properties. Their steady state fluorescence was measured in a Horiba NanoLog Spectrofluorimeter System with a Xe arc lamp as the excitation source and a monochromator set to 400 nm. Time resolved fluorescence was measured in the same setup, equipped with a time correlated single photon counting (TCSPC) system and a Horiba NanoLED pulsed light source (350 nm, 10 MHz repetition rate).

Data analysis. For each 'bright' spot where data was collected to analyze emitter properties, an identical experiment was performed in a 'dark' nearby location to subtract any background counts from the emission spectra, and to account for photons detected by the APD apart from the emitters' photoluminescence. This is important due to a small 250 Hz signal on top of a sizable 1 kHz background. Using a local background as explained above implies that the spectral data for a blank spot is flat and is thus not presented. The signal from a single molecule is low due to a low photoluminescence quantum yield (0.1-0.17) of the TADF emitter in these hosts. Additionally, the background signal is large due to the short excitation wavelength needed to excite the blue-green TADF emitters. Although the excitation wavelength is only resonant with the very tail of the host absorption profile, the large intensity of the excitation and the large number of host molecules (compared to a few emitters) results in a non-negligible fluorescence background from the host. Thus, the background displays a correlation with micro-time (Fig.

S2). From the raw histograms of micro-times for 'bright' spots (background + emitter fluorescence), an appropriately-scaled background curve was subtracted. This background curve was constructed from the raw histogram of micro-times measured at a nearby location over 300 s. Below we present three examples of raw and subtracted data for single 2PXZ-OXD molecules in PMMA (Fig. S2) with an integration time of 300 s or both signal and background.

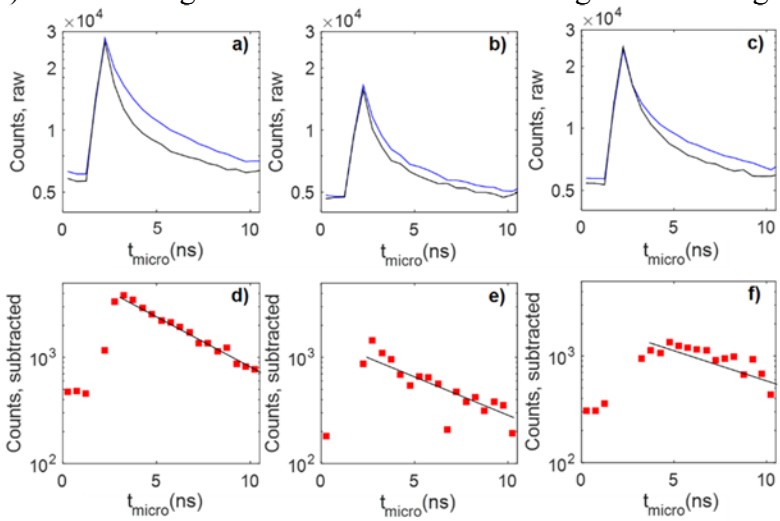

Figure S2. (a-c) Raw data for time resolved fluorescence of single 2PXZ-OXD emitters in PMMA. Data from the emitter is shown in blue, and a nearby background spot is shown in black. (d-f) Data after background subtraction for the same spots in (a-c).

B. Unperturbed photoluminescence dynamics in single-molecule measurement regime

The large dynamic range spanned by the prompt (1-10 ns) and delayed (1-100 μs) fluorescence decays of TADF emitters must be considered when studying their photophysics. When studying the prompt dynamics within the 13.2 ns time window allowed by the excitation laser repetition rate (75.9 MHz), any photons emitted through the delayed pathway will constitute a "background" component that is practically flat at these much faster time scales. These delayed photons contribute a small signal since for most TADF emitters the branching ratio from the excited singlet between fluorescence and intersystem crossing is 7:1.[1] When multiple exponential decays are observed over a finite time window that "folds" longer values onto the observation window, the leading perturbation is to increase the relative amplitude of the short component with respect to the longer ones, with minimal effects on the measured time scales.[2] We cross-checked our time-resolved single-molecule fluorescence data by comparing the PL decay of bulk samples obtained with the microscope to those obtained with a tabletop fluorimeter that uses a lower power and lower repetition rate excitation source. We measure two decay components for 2PXZ-OXD in either host: a fast 1.9 ns (1.6 ns) and a slow 12.5 ns (14.9 ns) when diluted in PMMA (polystyrene), as obtained with bi-exponential fits to the PL transients. These bi-exponential decays could be due to multiple populations of emitters in these bulk samples, given that the measured single-molecule or single-aggregate decays are mono-exponential. Furthermore, the signal-to-noise ratio of single-molecule data is sufficiently low compared to bulk fluorimetry that even if there were two components it would be difficult to distinguish them For the reasons previously stated, we observe no significant differences in the PL decay between the two setups (Fig. S3).

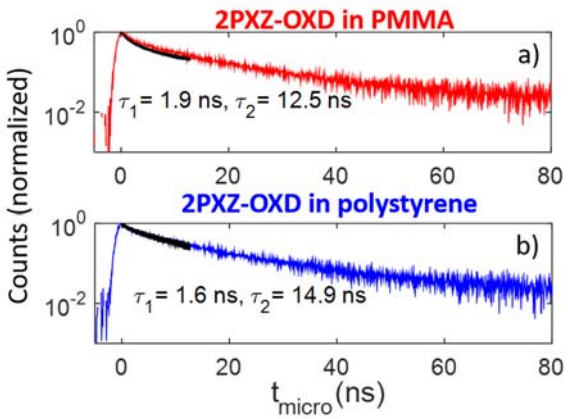

Figure S3. Photoluminescence decays of concentrated 2PXZ-OXD in PMMA (a) and polystyrene (b) measured in a tabletop fluorimeter are shown in red and blue, compared to the measurements in the microscope setup, in black.

C. Determination of number of emitter molecules in excitation volume

The blinking dynamics of clusters of emitters allow us to measure values of the detected photon count rate corresponding to different number of bright emitters. Analyzing the spacing between these brightness levels is a way to determine the increase in the detected photon count rate due to the addition of a single bright emitter. These blinking dynamics for a cluster with three brightness levels are shown in Fig. S4a.

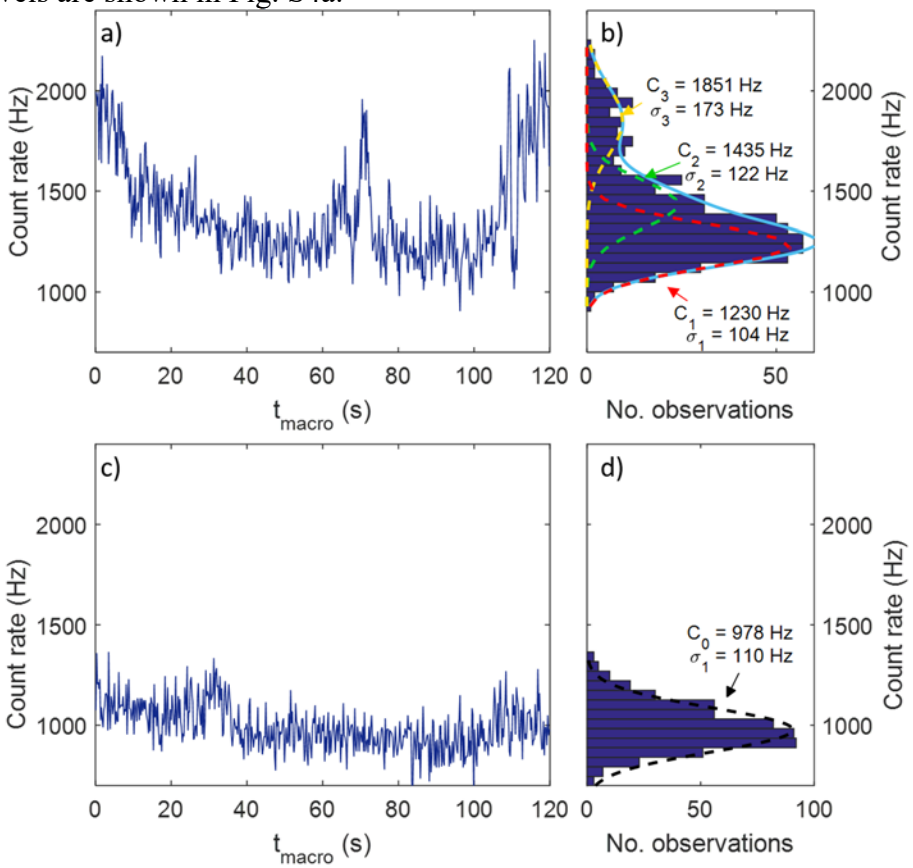

Figure S4. (a) Brightness as a function of macro-time for a measurement spot displaying three brightness levels, as shown in the accompanying histogram (b). The measured brightness of a background ('dark') spot is also shown as a function of macro-time (c) and a histogram (d).

In Fig. S4b, we present a histogram of the measured count rates for the trace shown in Fig. S4a. This distribution of count rates is described by three distinct levels, as detailed by the Gaussian lineshapes centered at 1230 Hz, 1453 Hz, and 1851 Hz. Performing the same analysis on several spots allows us to identify the different brightness levels and the spacing between them, as shown on Table S1. The average spacing between adjacent brightness levels is ≈ 250 Hz, which we use in the rest of the analysis as the count rate associated with a single emitter. Technically, the above analysis enables us to determine an approximate 'quantum' of brightness of ~250 Hz to tell the difference between n and n+1 emitters, but in order to determine the absolute number of emitters in a cluster we need to identify the count rate detected when no emitters are on (e.g., excitation leak-through, small amount of host fluorescence). This can be done by performing a similar analysis as above in a "dark" spot of a sample (Fig. S4c-d). We find that this background count rate is 978 Hz, and thus a single emitter would result in a detected count rate of ≈1.22 kHz (C_1 in Table S1).

Spot	C_0 (kHz)	C_1 (kHz)	C_2 (kHz)	C_3 (kHz)	C_4 (kHz)
A		1.23	1.45		1.85
B			1.42	1.62	1.91
C		1.23		1.61	1.86
D	1.09	1.35			1.96
E	1.07	1.28		1.65	1.93

Table S1. Values for the discrete brightness levels observed for several measurement spots for 2PXZ-OXD in polystyrene, used to determine the brightness associated with an individual emitter.

We performed the above Gaussian lineshape brightness level analysis on a subset of spots in which clear blinking was observed and that displayed significant stretches of macro-time at each level. This allowed for better accuracy in fitting Gaussian curves to individual brightness levels, but limited this in-depth analysis to 6 interrogated spots. Since the sum of different normally-distributed variables has a different variance than their individual widths and is dependent on the amount of correlation between the variables, here we use a different width for each of the Gaussian profiles used in our fits (Fig. S4b). This allows us to account for the possibility of different individual molecules having a slightly different brightness. Next, to ascertain the emitter numbers within the remainder of interrogated spots, we classified each spot based on the maximum count rate observed during the macro-time observation window in increments of 250 Hz above the background level. Finally, as a check, we collected the measured count rates for a representative set of 42 spots in polystyrene and 36 spots in PMMA and described them with a sum of Gaussian components at 0 Hz (background), and brightness levels at 250 Hz, 500 Hz, and 750 Hz (Fig. S5). Because the dashed curves that trace out the sum of these Gaussian components in Fig. S5a and b nicely follow the corresponding histogram profiles, we corroborate that the brightness levels obtained for the 6 spots considered in more detail reflect the blinking dynamics in the full population of single molecules and aggregates.

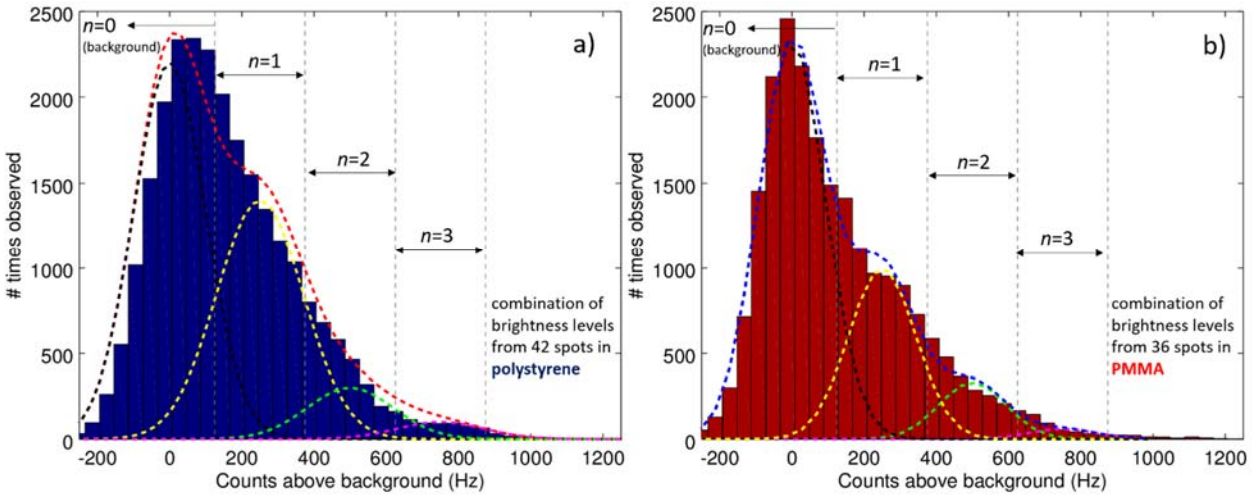

Figure S5. Number of 0.5-s time windows that a certain count rate, above background, was observed in the combined macro-time brightness traces for a collection of 42 spots in polystyrene (a) and 36 spots in PMMA (b). The bar charts show the histogram of all observed count rates, and the blue/red dotted lines show the results of a fit to a sum of Gaussians. Individual Gaussian components are shown for background (black), as well as levels corresponding to a n=1 emitter at 250 Hz (yellow), n=2 emitters at 500 Hz (green), and n=3 emitters 750 Hz (magenta).

To further validate this analysis, it is useful to estimate the expected count rate our fluorescence microscope setup would detect given the experimental conditions. An excitation beam with a power of $P \approx 15$ μW at the back of the microscope objective, and a wavelength λ=415 nm, has a photon flux $\Phi = P\lambda/hc$ is $\Phi \approx 3\text{x}10^{13}$ photons/s. If the beam is focused to a spot with a waist $\sigma \approx 1.3$μm (e^{-1} area $A = 5\text{x}10^{-8}$ cm^2), and the absorption cross-section for a 2PXZ-OXD molecule is $\sigma_{abs} \approx 2\text{x}10^{-17}$ cm^2, the rate at which the chromophore is excited is $k_{exc} \approx \Phi\, \sigma_{abs} / A \approx 12$ kHz (0.015% of the laser repetition rate). If we assume the fluorescence quantum yield of the emitter is $\eta_{QY} \approx 0.1$, the rate at which photons are emitted by the molecule would be $k_{em} = k_{exc}\eta_{QY} \approx 1.2$ kHz. Finally, we must include the collection efficiency of the microscope (i.e., collection solid angle, absorption and reflection losses), which we estimate at $\eta_{col} \approx 0.1$. This results in an estimated count rate of $k_{det} \approx 120$ Hz, which is on the same order of magnitude as the analysis above.

Given the breadth of the distributions in Figs. S4 & S5, the count rate level associated with n bright emitters is not a single number, but a "band" (e.g., due to various dipole orientations in the sample). We place these cutoffs at (n*250)±125 Hz above the background level. For example, a single bright emitter corresponds to count rates between 125 Hz and 375 Hz above background, two bright emitters to 375 Hz to 625 Hz above background, and so on.

It is also helpful to estimate the confidence bounds of assigning a given cluster size n. We start by calculating the probability of an emitter being in the bright state, taking the ratio of the time all observed single molecules are bright to the total observation time, and obtain $p_{ON} \approx 0.24$. Next, we calculate the probability of observing n bright emitters out of a cluster of size m, if each individual emitter has a probability p_{ON} of being bright. This probability, p, is given by a binomial distribution with n successes out of m events, each with success probability p_{ON}

$$p(n; m, p_{ON}) = \frac{m!}{n!(m-n)!}(p_{ON})^n(1-p_{ON})^{m-n} \quad \text{Eq. S1}$$

Similarly, the probability p' of observing more than n bright emitters in a cluster of size $m>n$ can be calculated as

$$p' = \sum_{j=n+1}^{m} \frac{m!}{j!(m-j)!} (p_{ON})^j (1-p_{ON})^{m-j} \quad \text{Eq. S2}$$

If we observe a given cluster M times and we never observe a brightness level larger than that corresponding to n emitters, we are interested in the probability that the cluster size is actually larger than n. Using the value of p' calculated above, the probability that a cluster of actual size s is observed M times but never has a brightness larger than n is

$$p_s = p(0; M, p') = (1-p')^M \text{ Eq. S3}$$

Since the probability of a cluster of size $s < n$ displaying a brightness $\geq n$ is zero, we can calculate the expected size of a cluster by summing over all values $s \geq n$

$$\langle S \rangle = \sum_{s=n}^{\infty} s\, p_s \text{ Eq. S4}$$

Using Eqs. S1-S4 we can calculate the expected cluster size for a sample that has been observed 20 times without observing a brightness level larger than that of a single molecule. We obtain $<S> = 1.3$, and there is a 75% chance that the actual size of the cluster is S=1 (and 25% that it is any other number greater than 1).

D. Aggregates are more likely than co-located individual emitters

When our microscope setup detects a brightness level associated with multiple chromophores, it can be due to two possibilities: (1) we are illuminating an aggregate composed of multiple emitters that are in close molecular contact, or (2) the excitation volume includes multiple independent emitters which happen to be in close proximity to each other due to the non-uniform concentration of dopants in the sample. To discount the latter possibility, here we discuss the probability of observing a density fluctuation that results in n emitters being located within a volume V.

If our sample contains a total number of emitters N in a volume V_t, the emitter density is $\rho = N/V_t$. Throughout this calculation we assume that we operate in the thermodynamical limit, where $V_t \rightarrow \infty$ and $N \rightarrow \infty$ but ρ is finite. Thus, the probability of finding one dye inside a test volume V is $p_1 = \rho V$. When placing N emitters, we are interested in the probability of n "successes" placing dyes in the same volume

$$\hat{p}_n = \frac{N!}{n!(N-n)!} {p_1}^n (1-p_1)^{N-n} \text{ Eq. S5}$$

In the dilute limit $p_1 \ll 1$, a reasonable assumption for samples prepared at the 10^{-12} M concentrations used in single-molecule experiments. Also, $N \gg n$ yields
the probability of finding n emitters inside a volume V, in a sample with a low emitter concentration given by

$$p_n = \frac{(\rho V)^n}{n!} e^{-\rho V} \quad \text{Eq. S6}$$

In our case, the microscope can probe molecules throughout the entire thickness of the film, so we use areal densities instead of volumetric densities. In our samples, the average spacing between emitters (D) and excitation beam diameter (d) are different in the data for 2PXZ-OXD in PMMA and in polystyrene (due to sample-to-sample variability in preparation conditions and day-to-day fluctuations in the collimation of the excitation beam). In PMMA, $D \approx 2.5$ μm and $d \approx 0.75$ μm; this results in a probability of having two co-localized emitters of $p_2 \approx 0.37\%$, a factor of 22X smaller than the probability of a single emitter in the excitation volume is $p_1 \approx 8.2\%$. In polystyrene, $D \approx 5$ μm and $d \approx 1.3$ μm; so the probability of having two co-localized

emitters is $p_2 \approx 0.2\%$, a factor of 32X smaller than the probability of a single emitter in the excitation volume is $p_1 \approx 6.3\%$.

These calculations support the statement that it is very unlikely that we observe clusters of size $n>1$ where emitters are randomly co-localized within the focal volume. It is much more likely that these spots with higher brightness are a result of intermolecular forces between emitters that result in aggregates, where emitters are in close molecular contact. These aggregates are likely formed in solution and then embedded in the solid polymer film during casting, therefore it will be important to monitor the tendency to aggregate for emitters in different hosts.

E. Fluorescence rate distributions for single molecule emitters

As discussed in the main text, static and dynamic disorder in the polymer host can affect the fluorescence rate of emitters. These effects can be due to perturbations in the dielectric environment of the emitter, fluctuations in the guest-host interactions that can change the rate of internal conversion, or by allowing/forcing the emitter to adopt a variety of molecular configurations (e.g., twist angle between donor-acceptor moieties). The time scales on which these configurations and environments change are usually separated into fast and slow processes. Time-invariant heterogeneities and processes that are much slower than the observation time appear as static disorder. Processes with time scales comparable to or faster than the observation time result in time-dependent observables and are referred to as dynamic disorder and can also display significant spatial heterogeneity. When analyzing fluctuations due to a large number of variables, such as all of the individual processes (radiative and nonradiative) that together determine the observed PL decay, it is more useful to consider their effects on the total rate where these fluctuations are additive ($k_{tot}=\Sigma k_i$), rather than the lifetime, where $1/\tau_{tot}=\Sigma(1/\tau_i)$. Below we explore the type and amount of disorder present in our samples by measuring the fluorescence rate of single emitters.

For each single emitter, we track the number of detected photons as a function of macro-time to determine the time periods when they are in the ON state, and then measure their fluorescence rate in 2 s intervals within those time periods. These values are grouped and a distribution is constructed for each emitter (Fig. S6). Due to blinking, some emitters are bright for a different amount of time than others, as reflected in the different number of observations for each one. Within the 300 s observation window, the lowest number of times a fluorescence rate was measured for a single emitter was $N=7$ (spots with fewer observations were not included in the analysis), while other emitters were measured as many as $N=79$ times ($\langle N \rangle = 26$). The shape and width of these distributions are not due to timing jitter, as their mean positions reflect differences corresponding to multiple nanoseconds in PL lifetime (e.g., 3.6 ns in Fig. 3e and 6.3 ns in Fig. 3a), which are an order of magnitude larger than the narrow IRF of the experimental setup (192 ps FWHM, Fig. S1). The width of the distributions (e.g., 0.035 ns^{-1} in Fig. 3b reflects a lifetime breadth of 0.82 ns), is also considerably larger than the IRF width.

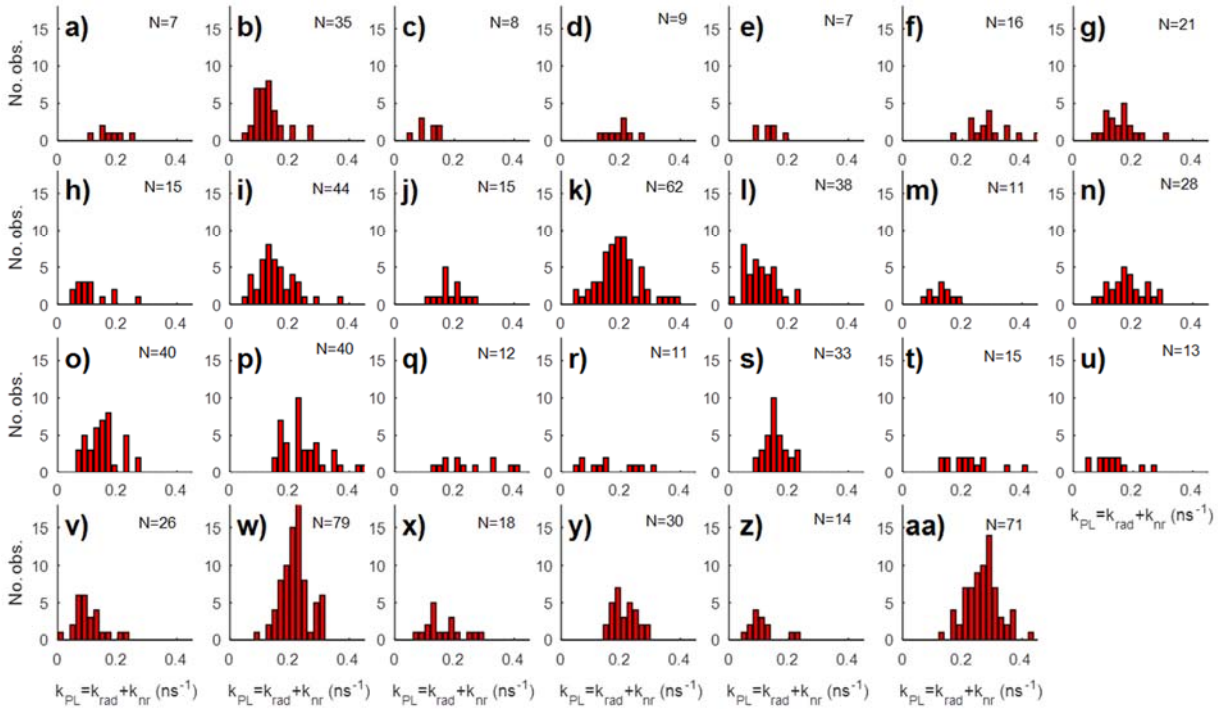

Figure S6. Distributions of instantaneous fluorescence rate measured in 2 s windows while emitters are on, for each interrogated single 2PXZ-OXD emitter in PMMA that resulted in N≥7 observations.

As the distributions in Fig. S6 show, we observe a sizable variation in the fluorescence rates between different emitters, but also a noticeable amount of fluctuation within a single distribution. To avoid biasing of these distributions by outliers, and in order to estimate the broadening of these distributions as a result of the uncertainty in the measured k_{PL} due to a limited number of photons, Poisson noise, and fitting uncertainty, we employed a kernel density estimator analysis. In this analysis, we build a distribution from unit-area Gaussian curves whose mean is the calculated rate value and whose standard deviation is the uncertainty in the rate value. Values with large uncertainties are thus prevented from biasing the distribution. In Fig. S7 we compare the histogram of the measured k_{PL} rates for several single molecules (in red) to the kernel density estimation (green). In each case, the two distributions match well.

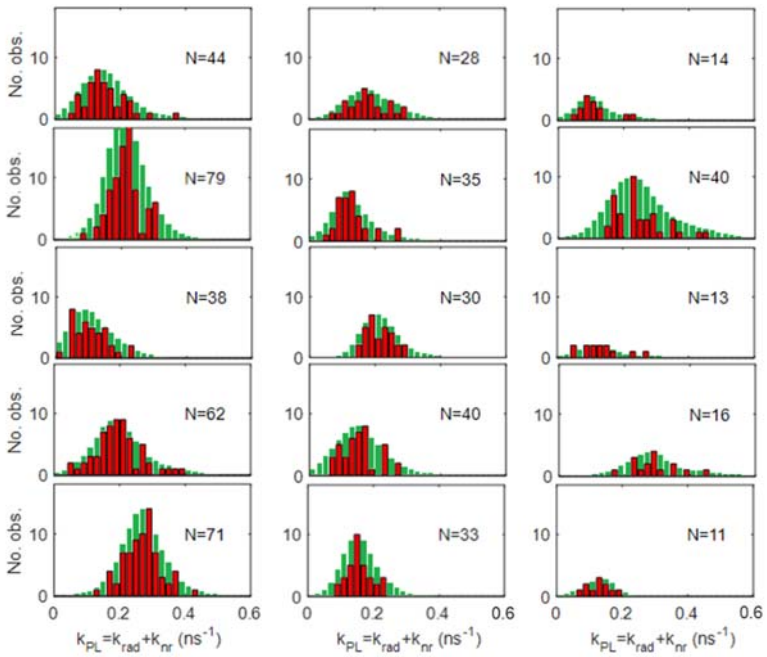

Figure S7. Distributions of PL decay rates of 2PXZ-OXD single molecules in PMMA, comparing the results described in the text (red) to the kernel density estimation (green). No additional broadening is observed. The distributions shown in the left column of this figure are those in Fig. 3 in the main text.

Additionally, we have compared the standard deviation of the measured set of k_{PL} for each emitter (σ_{rates}) to the mean error for the same set of measured rates (μ_{error}). As shown in Fig. S8, $\sigma_{rates}>\mu_{error}$ in all but 3 cases. The measurement uncertainty has a non-negligible contribution to the width of a k_{PL} distribution in a single emitter and is due to the limited number of photons measured to obtain each 'instantaneous' decay rate. If a single emitter were to have a well-defined and constant k_{PL} value, the measurement-related breadth of the observed k_{PL} distribution could be as low as 0.029 ns^{-1} for a bright emitter or 0.063 ns^{-1} for a dim one. These breadths are typically smaller than the widths of the measured distributions (0.034 – 0.093 ns^{-1}) and the range spanned by the mean values (0.103 – 0.183 ns^{-1}). Therefore, the combined intrinsic and instrument-related broadening of the k_{PL} distributions are not large enough to prevent the observation of different centers of the distributions; these differences are related to static disorder in the sample and emitter properties.

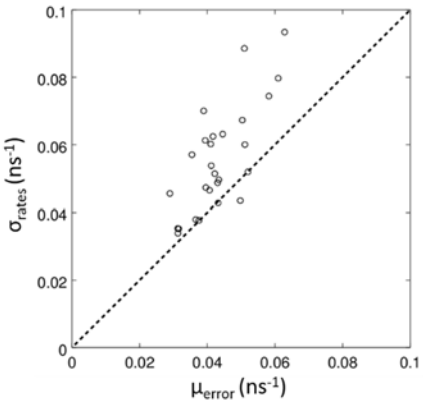

Figure S8. Comparison of the broadening of the distribution of measured rates (σ_{rates}) to the mean error for the measured rates (μ_{error}). The standard deviation of the measured rates is larger than the uncertainty in their values.

Before describing the pattern that emerges from the fluorescence rate distributions in Fig. S6, it is helpful to detail how various effects might be displayed in the data. Static disorder in the host-guest environment would be reflected as a different mean value $\langle k_{PL} \rangle$ for each measured emitter. As for dynamic disorder, small changes in the emitter conformation or polymer packing that do not drastically change the equilibrium stat of the host-guest complex can be reflected in fluctuations of k_{PL} around their average value, widening the distribution. Larger conformational changes in the emitter and/or surrounding host would substantially change the properties of the emitter and shift the mean of the distribution to a different equilibrium value. If these large changes occur in the process of our measurement, we would observe a double-peaked or unusually broad distribution. Since the distributions are almost identical when the uncertainty in the measured rate is included through a kernel density estimator analysis, and we generally observe a larger breadth in the k_{PL} distribution than that expected from shot noise, we interpret these data as evidence that the broadening of the distributions is not entirely determined by measurement uncertainty. Thus, the 'instantaneous' k_{PL} distributions display additional broadening as a result of fluctuations in the sample due to dynamic disorder, as well as distinct mean values that reflect a sizable contribution of static disorder.

In Fig. S6, we notice that distributions that are significantly broader or potentially displaying more than one peak are rare (Fig. S6 k, q, r). However, the mean of the distributions vary significantly. There are a number of instances with a small mean value $\langle k_{PL} \rangle < 0.2$ ns^{-1} (Fig. S6 c, e, h, i, l, m, s, u, v, z); others have a larger value $\langle k_{PL} \rangle > 0.2$ ns^{-1} (Fig. S6 f, p, aa); yet another group could be considered as a medium mean value $\langle k_{PL} \rangle \approx 0.2$ ns^{-1} (Fig. S6 g, j, k, n, s, t, w, x, y). Thus, the most noticeable characteristic of the distributions in Fig. S6 is their different $\langle k_{PL} \rangle$ values due to a dominant role of static disorder.

Performing the equivalent analysis of the single 2PXZ-OXD emitters in polystyrene yields the distributions shown in Fig. S9. The smaller number of observations prevents being conclusive, but one can see the presence of the heterogeneity clearly seen in PMMA. The distributions shown in Fig. S9a,j are clearly different from those in Fig. S9c,h,k and Fig. S9d.

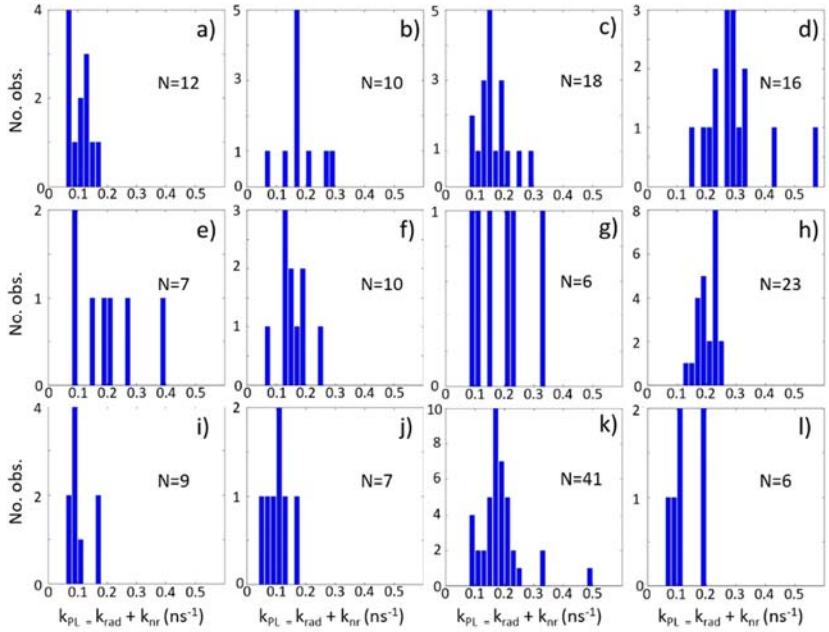

Figure S9. Distributions of instantaneous fluorescence rate measured in 2 s windows while emitters are on, for all interrogated single 2PXZ-OXD emitters in polystyrene that resulted in $N \geq 6$ observations.

F. Determination of radiative and nonradiative decay rates from time-resolved fluorescence data

As detailed in the main text, we used the measured fluorescence rate and the number of detected photons in order to calculate the radiative and nonradiative rate components for each observation. In this section, first we describe how we test the assumption used in our analysis that all single molecules share a common prompt PLQY, and second, we present scatter plots analogous to those in Fig. 4a of the main text for each of the contributing single molecules.

Testing assumption of common prompt PLQY: In the analysis leading to Eqs.1-2 and Fig. 4, we assumed that the distribution of 'instantaneous' (over a 2 s observation interval) prompt PLQY values for 2PXZ-OXD in PMMA had a mean of 0.17. This analysis yielded a set of prompt PLQY values with a standard deviation of 0.05. To test the effects of this assumption, we provide a supplemental analysis here. Instead of assuming the average prompt PLQY of each molecule was 0.17, we give each emitter an average prompt PLQY with a randomly-selected value out of a Gaussian distribution with mean 0.17 and standard deviation σ_{QY}=0.05. Relaxing our assumption in this way results in a k_{nr} vs k_{rad} scatter plot that is slightly broadened, but the general trend remains the same (Fig. S10a). Further increasing the variability in the average prompt PLQY for a single molecule to σ_{QY}=0.075 and keeping the same mean results in the scatter plot shown in Fig. S10b. Even for such a large variability (44% of the mean), the general positive trend remains visible – although a more significant broadening is also evident. We take these test results to mean that our assumption in Eq. 1 of each molecule possessing the same average PLQY is not altering our conclusions as compared to what one would obtain by allowing the average PLQY to vary from molecule to molecule. While our assumptions do not include molecule-to-molecule variation in the average PLQY, they minimize the effects of different emitter orientations coupling more or less to a fixed-polarization excitation laser field.

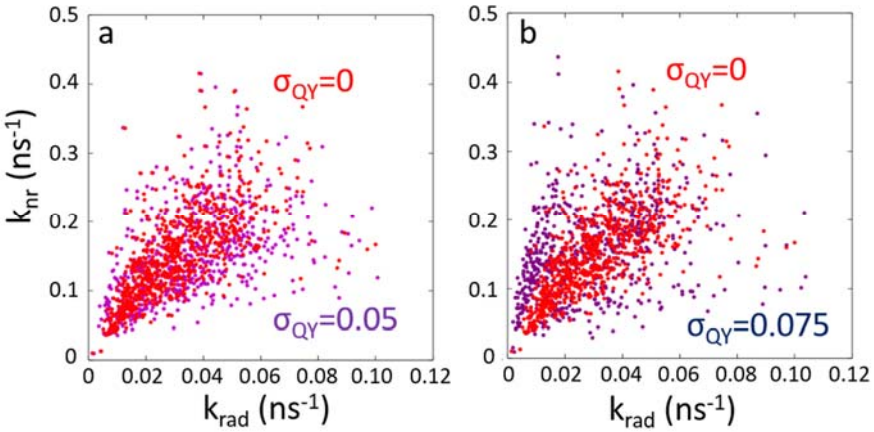

Figure S10. Effect of prompt PLQY variability on the observed k_{nr} vs k_{rad} trends. Comparison between the case discussed in the main text, where each single molecule is assumed to have the same $PLQY=PLQY_{bulk}$ ($\sigma_{QY}=0$, in red) to a situation in which the average prompt PLQY for each single molecule is drawn from a Gaussian distribution of increasing width: (a) $\sigma_{QY}=0.05$, in magenta; (b) $\sigma_{QY}=0.075$, in purple.

While our assumption regarding the mean PLQY for each molecule affects the position of its data 'cloud' in the k_{rad}-k_{nr} scatter plot, its shape is determined by the directly measured brightness and decay rate (e.g., see differences between Fig. S10f,t,w,aa) and is therefore not compromised by our assumption in any event.

Single molecule scatter plots: While different dipole moment orientations prevented us from describing the differences between emitters in more detail, here we present each emitter's contribution to the data compiled in Fig. 4a in the main text. In Fig. S11 below, each panel has the data compiled for all single emitters in PMMA, as shown in Fig. 4a, but highlights the data points belonging to each individual emitter.

The observations in the lower left corner of the plots in Figs. 4a and S11 are those with low k_{rad} and k_{nr}, associated with the small oscillator strength and host-guest interactions of a 'twisted' molecular conformation that is conducive to efficient TADF. Conversely, those observations in the upper right corner display a high k_{rad} and k_{nr}, associated with the larger oscillator strength and stronger host-guest interactions of a 'planar' molecular conformation that prevents the formation of an intramolecular charge transfer state required for efficient TADF. Interestingly, some emitters' data is clustered in the lower left corner (Fig. S11 b, c, l, m, v, z), while others' are clustered in the upper right corner (Fig. S11 f, p, w, y, aa), and a few emitters' rates span the entire range (Fig. S11 k, n). The selection of host materials and processing conditions that bias the distribution of host-guest configurations to those with low k_{rad} and k_{nr} will prove crucial in the development of efficient TADF-based OLEDs.

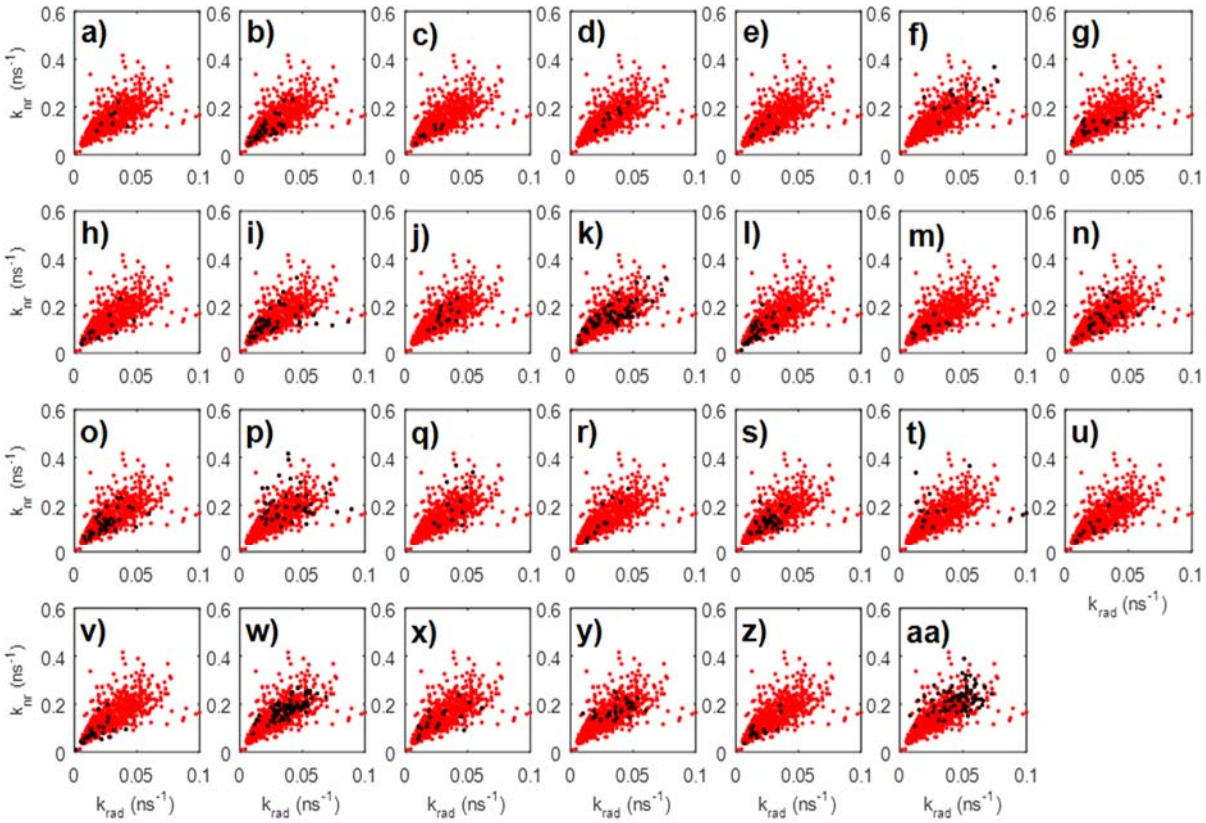

Figure S11. Compiled data of radiative and nonradiative rates for all single-molecule measurements of 2PXZ-OX in PMMA is shown in red, and the data points corresponding to each individual emitter are shown in black for each panel.

The contribution from each individual emitter to the compiled data in the k_{nr} vs k_{rad} plot when using polystyrene as a host are shown in Fig. S12. Again, we observe emitters whose data clusters in the lower left corner that is associated with 'twisted' conformations (Fig. S12a,c,i,j,l), or in the upper right region of the plot ('planar' molecules, Fig. S12d,), while others appear to span both configurations (Fig. S12b,e,k). These observations of 2PXZ-OXD in polystyrene are affected by the detrimental effects of a low PLQY, which prevents conclusive statements of individual molecules; thus we focused our discussion on the trends in the compiled data as shown in Fig. 4a.

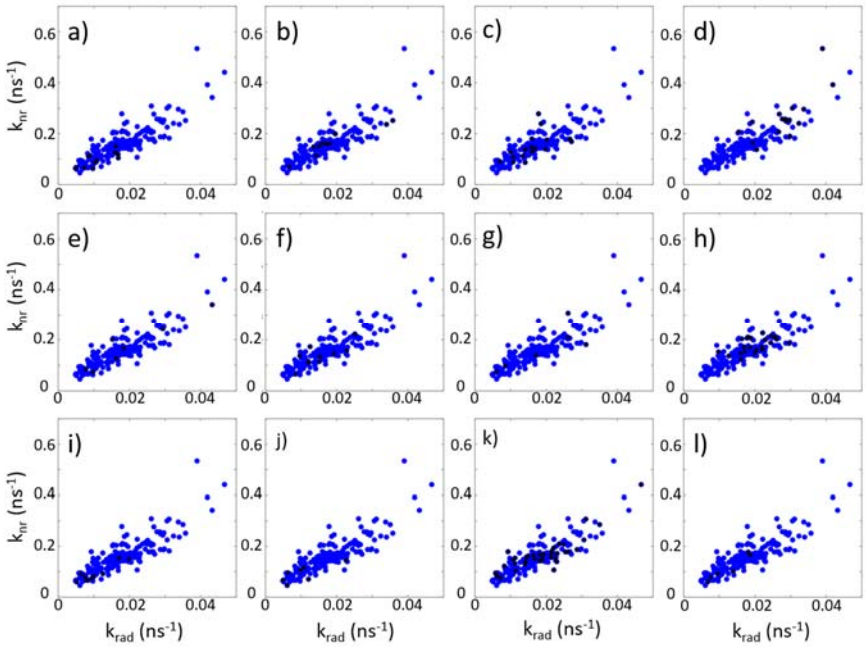

Figure S12. Compiled data of radiative and nonradiative rates for all single-molecule measurements of 2PXZ-OXD in polystyrene is shown in blue, and the data points corresponding to each individual emitter are shown in black for each panel.

G. Effect of aggregate size on fluorescence lifetime distributions

Since the assignment of aggregate size is dependent on the observation of a given brightness level (dependent on molecular orientation) and blinking dynamics, there is a possibility of error in the determined aggregate size. The purpose of our analysis is to identify single emitters and to isolate their statistics from those of aggregates. Here we compare the distributions of τ_{PL} from Figure 5 in the main text when only the spots that are assigned to single molecules are considered (Fig. 5a,d) to the distribution of all observed lifetimes (Fig. S13), where the information from spots with single molecules and aggregates ($n \leq 3$) is included. The distributions do narrow when incorporating the aggregates, consistent with the discussion in the main text.

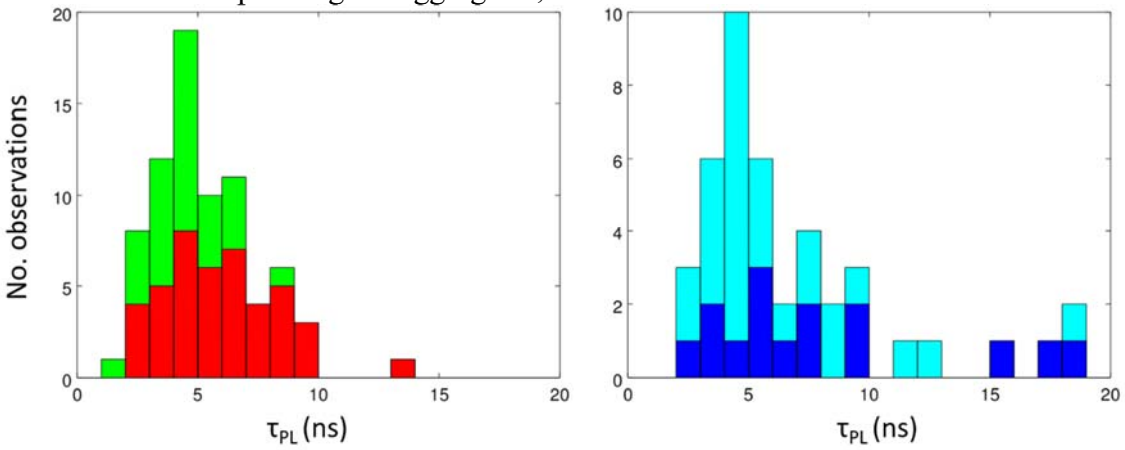

Figure S13. Distribution of fluorescence lifetimes for 2PXZ-OXD molecules. (a) In PMMA, comparing single-emitters only (red) to a combination of single-molecules and aggregates (green). (b) In polystyrene, comparing single-emitters only (dark blue) to a combination of single-molecules and aggregates (cyan).

Annihilation of excitations within these small aggregates plays a minor role, as the probability of having multiple excitations in a single aggregate is low at the excitation rates used for single-photon detection by a TCSPC card. In fact, solving the kinetic model (see part H of SI below) of the state manifold for an aggregate of size n=3 shows that the combined occupancy of the excited states is never above 0.305.

H. Analysis of singlet-triplet equilibration dynamics and FCS experiments and simulations

One of the most important issues in TADF materials is the tuning and determination of ΔE_{ST}, as it is a critical parameter in enabling RISC. The two methods of luminesce of interest in these systems are photoluminescence and electroluminescence, which differ in the ratio of initial excitations that are singlets or triplets. Comparing the photoluminescence and electroluminescence quantum yields (PLQY and ELQY respectively) of a system that includes singlet-triplet cycling and nonradiative triplet decay, one finds that the electroluminescence of a system with efficient triplet to singlet conversion can still exceed the photoluminescence of an otherwise equivalent system in which k_{RISC}=0, i.e. in which there is no delayed fluorescence. This observation underscores the technical relevance of TADF. The prompt portion of the PLQY can be defined as $PLQY_{prompt}$= PLQY(k_{RISC}=0), and the ELQY is then given by

$$ELQY = \left[\frac{\frac{1}{4}(1+3\eta_{RISC})}{1-\eta_{ISC}\eta_{RISC}}\right] PLQY_{prompt}, \quad \text{Eq. S7}$$

where $\eta_{RISC} = \frac{k_{RISC}}{k_{RISC}+k_{td}}$, $\eta_{ISC} = \frac{k_{ISC}}{k_{PL}}$, and $k_{PL}=k_{rad}+k_{IC}+k_{ISC}$. Using these expressions, and assuming an Arrhenius dependence of forward/backward intersystem crossing $k_{RISC}=k_{ISC}\exp(-\Delta E_{ST}/k_BT)$ for the situation with non-zero k_{RISC}, the above mentioned ELQY(k_{RISC})>PLQY(k_{RISC}=0) crossover can be computed to occur for $\frac{\Delta E_{ST}}{k_BT} < ln\left(\frac{4}{3}{\eta_{ISC}}^2\left(\frac{k_{PL}}{k_{td}}\right)\right)$. This inequality can be reduced to $\Delta E_{ST} \lesssim 5.5\ k_BT$ in a TADF system with typical characteristics such as $\eta_{ISC} = 13\%$, a PL lifetime of 10 ns, and a nonradiative triplet decay on a time scale of 100 µs.

Before discussing in more detail the observed singlet-triplet equilibration dynamics measured in our FCS experiments, it is useful to consider the potential contributions of experimental artifacts related to the use of a single detector. The APD detector used in these studies has an afterpulsing probability of 0.1-3%. APD afterpulsing has the effect of distorting the short-time FCS signal—typically at or below 1-10 µs. An FCS signal with significant afterpulsing shows a steep rise at the characteristic afterpulsing time.[3,4] To a first approximation, if the cluster FCS traces displayed a noticeable afterpulsing artifact, a second decay component would be required to fit the autocorrelation trace.[3] This situation would reduce the confidence in the fitted τ_{FCS} (more fitting parameters) and could also artificially reduce its value (due to a spurious increase in autocorrelation amplitude at short times). In the autocorrelation curves measured, we observe no strong contribution from afterpulsing (Fig. 6).

To confirm that the time scales of singlet-triplet equilibration measured in the FCS experiments are reasonable, we use a Monte Carlo simulation of the excited state dynamics in a TADF system, with realistic time constants extracted from the literature.

For these Monte Carlo simulations, we implement an algorithm that creates n emitters (here, n=15) and initializes them in the ground state S_0. Each emitter is excited to the singlet state S_1 after a time dt_i has passed, randomly selected from an exponential distribution with mean $1/k_{ex}$. When an emitter is in the excited state, it can decay to the ground state or convert to a triplet (T_1) with a probability given by the branching ratios determined by the fluorescence rate k_{fl} ($k_{fl} = k_{rad} + k_{IC}$) and intersystem crossing rate k_{ISC}; after either of these processes occur, time is advanced by another step dt_i selected at random from an exponential distribution with mean $1/(k_{fl}+k_{ISC})$. When an emitter is in the triplet state, it can be converted back to S_1 (reverse intersystem crossing, RISC) after a wait time dt_i randomly selected from an exponential distribution with mean $1/k_{RISC}$.

We use an excitation rate of $k_{ex}= 2.5\text{x}10^4$ Hz (consistent with the 250 Hz detection rate as described above, $\eta_{QY} \sim \eta_{col} \sim 0.1$), a fluorescence rate $k_{fl}= 6.67\text{x}10^7$ Hz (fluorescence lifetime of 15 ns). The reverse intersystem crossing rate is set to $k_{RISC}= 2\text{x}10^4$ Hz ($\tau_{RISC}= 50$ μs), and we use detailed balance to obtain $k_{ISC}= 1.2\text{x}10^7$ Hz after estimating the singlet-triplet energy gap ΔE_{ST}=160 meV, at room temperature.

The observables in these simulations are the arrival time for each detected photon, and the time elapsed between excitation and emission for each detected photon. With these values we can construct a PL decay curve (Fig. S14a) and also calculate the autocorrelation function of the sample brightness (Fig. S14b) as performed for the experimental data shown in the main text (Fig. 6). The PL decay displays both a prompt and a delayed fluorescence component, with lifetimes determined by the interplay of rates connecting the $\{S_0,S_1,T_1\}$ state manifold. The prompt lifetime is given by the total rate at which population leaves S_1,

$$\tau_{prompt} = \frac{1}{k_{fl}+k_{ISC}} \quad \text{Eq. S8}$$

and the delayed lifetime is given by the time scale for a complete $S_1 \rightarrow T_1 \rightarrow S_1$ divided by the probability that each individual $T_1 \rightarrow S_1$ cycle results in fluorescence decay, given by the branching ratio of fluorescence to intersystem crossing

$$\tau_{delayed} = \left(\tau_{prompt} + \tau_{RISC}\right)\left(\frac{k_{fl}+k_{ISC}}{k_{fl}}\right) \approx \tau_{RISC}\left(\frac{k_{fl}+k_{ISC}}{k_{fl}}\right) \quad \text{Eq. S9}$$

It is worth noting that the relative number of photons arriving in the prompt or delayed fluorescence channel is determined by the initial branching ratio of each process from S_1

$$\frac{N_{delayed}}{N_{prompt}} = \frac{k_{ISC}}{k_{fl}} = \frac{A_{delayed}\tau_{delayed}}{A_{prompt}\tau_{prompt}} \quad \text{Eq. S10}$$

where A_{prompt} and $A_{delayed}$ are, respectively, the amplitudes of the prompt and delayed exponential components of the PL decay. For the simulation results shown in Fig. S14a, $A_{prompt}\tau_{prompt} \approx$ 18.8 ns and $A_{delayed}\tau_{delayed} \approx$ 3.3 ns, in agreement with the ratio $k_{ISC}/k_{fl} \approx 0.18$.

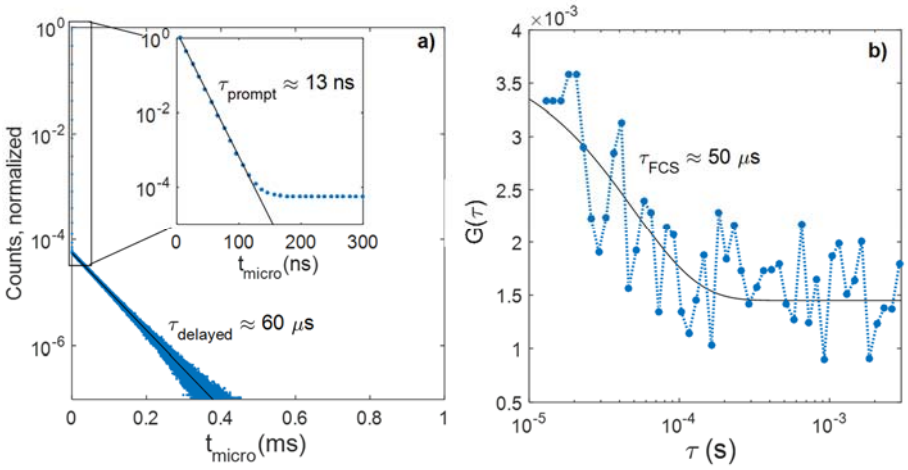

Figure S14. Results from Monte Carlo simulations of TADF dynamics showing the PL decay curve (a) calculated with the micro-time for each emitted photon, and the brightness autocorrelation function using the macro-time for each detected photon (b). We include the PLQY and collection efficiency in our simulation to allow more direct comparison to experimental data.

These Monte Carlo simulations are useful to compare to the observables in our experiments. The relative simplicity of the system of differential equations that determines the changes in population of ground and excited state also allows us to calculate analytical solutions.

$$\frac{d}{dt}(S_0) = -k_{ex}S_0 + k_{fl}S_1 \qquad \text{Eq. S11a}$$

$$\frac{d}{dt}(S_1) = k_{ex}S_0 - (k_{fl} + k_{ISC})S_1 + k_{RISC}T_1 \qquad \text{Eq. S11b}$$

$$\frac{d}{dt}(T_1) = k_{ISC}S_1 - k_{RISC}T_1 \qquad \text{Eq. S11c}$$

The coupled system of differential equations S11a-c is solved numerically by finding the eigenvalues and eigenvectors of the matrix

$$\begin{bmatrix} -k_{ex} & k_{fl} & 0 \\ k_{ex} & -(k_{fl} + k_{ISC}) & k_{RISC} \\ 0 & k_{ISC} & -k_{RISC} \end{bmatrix} \qquad \text{Eq. S12}$$

The eigenvalues λ_i and eigenvectors v_i are given by

$$\lambda_1 = 0, \quad \lambda_{2,3} = -\tfrac{1}{2}[k_{ex}+k_{fl}+k_{ISC}+k_{RISC} \mp \beta] \qquad \text{Eq. S13a}$$

$$v_1 = \begin{bmatrix} \frac{k_{fl}}{k_{ex}} \\ 1 \\ \frac{k_{ISC}}{k_{RISC}} \end{bmatrix}, \quad v_{2,3} = \begin{bmatrix} \frac{-2k_{fl}}{k_{fl}+k_{ISC}+k_{RISC}-k_{ex} \mp \beta} \\ 1 \\ \frac{-2k_{ISC}}{k_{ex}+k_{fl}+k_{ISC}-k_{RISC} \mp \beta} \end{bmatrix} \qquad \text{Eq. S13b}$$

where $\beta \equiv \sqrt{(k_{ex} + k_{fl} - k_{ISC} - k_{RISC})^2 + 4k_{fl}k_{ISC}}$. Each of these eigenvalues is the rate of an exponential decay that is multiplied by the respective eigenvector and an amplitude

$$\begin{bmatrix} S_0(t) \\ S_1(t) \\ T_1(t) \end{bmatrix} = A_1 v_1 e^{\lambda_1 t} + A_2 v_2 e^{\lambda_2 t} + A_3 v_3 e^{\lambda_3 t} \qquad \text{Eq. S14}$$

The amplitudes A_i are found by imposing the initial condition where all population starts in the ground state

$$\begin{bmatrix}1\\0\\0\end{bmatrix} = A_1 v_1 + A_2 v_2 + A_3 v_3 \qquad \text{Eq. S15}$$

The changes in the S_1 population will be related to the brightness of the sample and are proportional to the autocorrelation function $G(t)$. In the types of systems studied here, k_{fl} and k_{ISC} are much larger than k_{ex} and k_{RISC}, thus we are interested in the amplitude of the component associated with λ_2. Thus, τ_{FCS} is given by

$$1/\tau_{FCS} = \frac{1}{2}\left[k_{ex}+k_{fl}+k_{ISC}+k_{RISC}-\sqrt{(k_{ex}+k_{fl}-k_{ISC}-k_{RISC})^2+4k_{fl}k_{ISC}}\right] \quad \text{Eq. S16}$$

In our experimental regime, $k_{fl} \sim k_{ISC} \gg k_{ex}, k_{RISC}$. Therefore, we can simplify Eq. S16 to

$$1/\tau_{FCS} \approx k_{RISC} + \frac{k_{ISC}}{1+\left(\frac{k_{fl}+k_{ISC}}{k_{ex}-k_{RISC}}\right)} . \quad \text{Eq. S17}$$

Furthermore, if $k_{ex} \approx k_{RISC}$ then $\tau_{FCS} \approx 1/k_{RISC}$, as shown in Fig. S15. Therefore, the time scale τ_{FCS} obtained in both the Monte Carlo simulations and also in the FCS experiments can be considered to approximately correspond to the slowest (i.e., rate-limiting) timescale in the dynamics, namely the RISC time that limits the dynamics of equilibration between the excited singlet and triplet states.

It can also be shown that

$$A_2 = \frac{k_{ex}[k_{RISC}(k_{ex}+k_{fl}-k_{ISC}-k_{RISC}-\beta)+2k_{ex}k_{ISC}]}{2[k_{fl}k_{ISC}-(k_{fl}-k_{ex})(k_{ISC}-k_{RISC})]} \qquad \text{Eq. S18}$$

It is relevant to examine a special point of Eq. S18, which is that if $k_{ex}=k_{RISC}$, then $A_2=0$ (Fig. S15a). The value of A_2 when $k_{ex}>k_{RISC}$ is positive, and A_2 is negative if $k_{ex}<k_{RISC}$. This is relevant as one potential implication is that controlling k_{ex} and finding the value at which the autocorrelation function amplitude switches sign can be used to more accurately determine k_{RISC}. In our case, we are in the regime where $k_{ex}>k_{RISC}$ and within the region where the discrepancy between τ_{FCS} and τ_{RISC} is small (<10%), as shown in Fig. S15b.

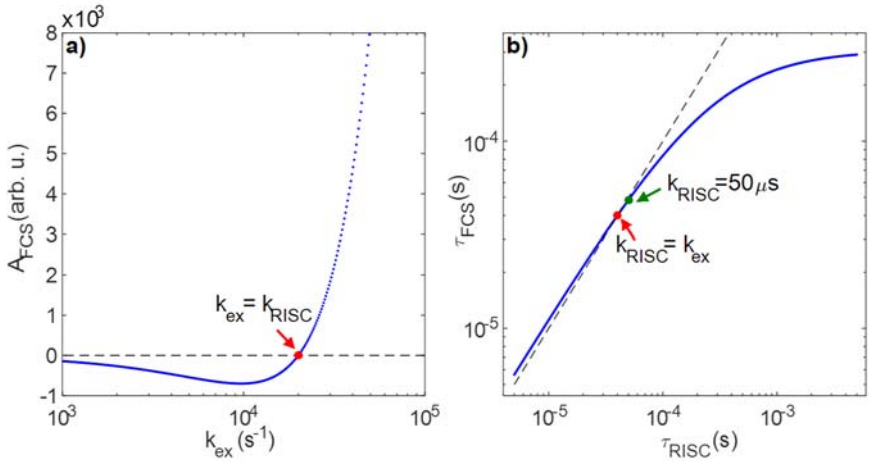

Figure S15. The analytical solution of the kinetic model in Eq. S11 leads to the observation that the amplitude A_{FCS} of the decay in the autocorrelation function $G(t)$ changes sign when $k_{ex}=k_{RISC}$ (a), and it allows the comparison of the resulting τ_{FCS} to the τ_{RISC} in the kinetic model (b). The dotted line in (a) marks the $A_{FCS}=0$ crossing. The dotted line in (b) is a line of slope 1 to show the deviation of the solution (orange) from $\tau_{FCS} = \tau_{RISC}$. The red circles in (a,b) highlight the $k_{RISC}=k_{ex}$ point, and the blue circle in (b) shows the conditions used in the Monte Carlo simulations.

I. References

(1) Lee, J.; Shizu, K.; Tanaka, H.; Nomura, H.; Yasuda, T.; Adachi, C. *J. Mater. Chem. C* **2013**, *1*, 4599.

(2) Leung, R. W. K.; Yeh, S.-C. A.; Fang, Q. *Biomed. Opt. Express* **2011**, *2*, 2517.

(3) Zhao, M.; Jin, L.; Chen, B.; Ding, Y.; Ma, H.; Chen, D. *Appl. Opt.* **2003**, *42*, 4031.

(4) Kapusta, P.; Wahl, M.; Erdmann, R. *Advanced Photon Counting: Applications, Methods, Instrumentation*; Springer, 2015.